RSC Advances

PAPER

View Article Online
View Journal | View Issue

Cite this: *RSC Adv.*, 2023, **13**, 30838

Fabrication of ternary metal oxide (ZnO:NiO:CuO) nanocomposite heterojunctions for enhanced photocatalytic and antibacterial applications†

Muhammad Zahid Ishaque,[a] Yasir Zaman,[a] Alia Arif,[a] Abu Bakar Siddique,*[b] Muhammad Shahzad,[fa] Daoud Ali,[c] Muhammad Aslam,[e] Hira Zaman*[d] and Muhammad Faizan[a]

In this article, ZnO:NiO:CuO nanocomposites (NCPs) were synthesized using a hydrothermal method, with different Zn : Ni : Cu molar ratios (1 : 1 : 1, 2 : 1 : 1, 1 : 2 : 1, and 1 : 1 : 1). The PXRD confirmed the formation of a NCP consisting of ZnO (hexagonal), NiO (cubic), and CuO (monoclinic) structures. The crystallite sizes of NCPs were calculated using Debye Scherrer and Williamson–Hall methods. The calculated crystalline sizes (Scherrer method) of the NCPs were determined to be 21, 27, 23, and 20 nm for the molar ratios 1 : 1 : 1, 2 : 1 : 1, 1 : 2 : 1, and 1 : 1 : 2, respectively. FTIR spectra confirmed the successful formation of heterojunction NCPs *via* the presence of metal–oxygen bonds. The UV-vis spectroscopy was used to calculate the bandgap of synthesized samples and was found in the range of 2.99–2.17 eV. SEM images showed the mixed morphology of NCPs *i.e.*, irregular spherical and rod-like structures. The dielectric properties, including AC conductivity, dielectric constant, impedance, and dielectric loss parameters were measured using an LCR meter. The DC electrical measurements revealed that NCPs have a high electrical conductivity. All the NCPs were evaluated for the photocatalytic degradation of Methylene blue (MB), methyl orange (MO), and a mixture of both of these dyes. The NCPs with a molar ratio 1 : 1 : 2 (Zn : Ni : Cu) displayed outstanding photocatalytic activity under sunlight, achieving the degradation efficiency of 98% for methylene blue (MB), 92% for methyl orange (MO) and more than 87% in the case of a mixture of dyes within just 90 minutes of illumination. The antibacterial activity results showed the more noxious nature of NCPs against Gram-negative bacteria with a maximum zone of inhibition revealed by the NCPs of molar ratio 1 : 2 : 1 (Zn : Ni : Cu). On the basis of these observations, it can be anticipated that the NCPs can be successfully employed for the purification of contaminated water by the degradation of hazardous organic compounds and in antibacterial ointments.

Received 31st July 2023
Accepted 11th October 2023

DOI: 10.1039/d3ra05170f

rsc.li/rsc-advances

1. Introduction

Water pollution is currently considered a global issue due to its harmful effects on human health, the environment, and aquatic life.[1,2] Despite the essential need for clean water and air for human survival, approximately 80% of industrial waste and municipal wastewater is discharged into the environment without treatment.[3] Organic dyes from industries, like plastic, textile, tanning, paper, and leather, contribute to water pollution as they are discharged directly to fresh water reservoirs.[4,5] Food industry wastewater enriched with microorganisms, responsible for many diseases, is being continuously mixed in lakes and agricultural land without any pretreatment.[6] In this regard, the development of cost-effective, eco-friendly, and easily reusable materials to eliminate these pollutants is needed.[7] These harmful pollutants can be eliminated from industrial effluents by adsorption, filtration, reverse osmosis, or photodegradation on a nanocatalyst surface,[8] ensuring the availability of clean and safe drinking water and preventing the spread of waterborne diseases.[9] However, photodegradation on a solid surface is considered a viable approach for all these applications due to the less expensive and robust nature of these materials.[10]

Nanomaterials have enormous applications in various fields, including optics, fuel cells, batteries, sensors, catalysis, energy

[a]*Department of Physics, University of Sargodha, Sargodha, 40100, Pakistan. E-mail: yasir.zaman@uos.edu.pk*

[b]*Institute of Chemistry, University of Sargodha, Sargodha, 40100, Pakistan. E-mail: abubakar.siddique@uos.edu.pk*

[c]*Department of Zoology, College of Science, King Saud University, PO Box 2455, Riyadh 11451, Saudi Arabia*

[d]*Institute of Chemical Sciences, University of Peshawar, Khyber Pakhtunkhwa, 25120, Pakistan. E-mail: hzamkhan@yahoo.com*

[e]*Institute of Physics and Technology, Ural Federal University, Mira Str.19, 620002 Yekaterinburg, Russia*

[f]*Northwestern Polytechnical Univerity, Xi'an, P. R China*

† Electronic supplementary information (ESI) available. See DOI: https://doi.org/10.1039/d3ra05170f

storage, and biomedical imaging.[11] Among the many nanomaterials, semiconductor metal oxide nanoparticles (NPs) such as ZnO,[12] TiO_2,[13] NiO,[14] CuO,[15] and SnO_2,[16] *etc.* as well as doped metal oxides,[17,18] have attracted great attention for antibacterial and photocatalytic applications due to their easily tunable properties. Many metal NPs have been studied for photodegradation of hazardous organic materials but the rapid electron/hole pair recombination in metal oxide is still the main problem that impedes photocatalytic activity.[19] However, the development of metal oxide NCP materials has greatly reduced the hurdles in the use of metal NPs as photocatalysts due to the high charge carrier separation, mobility of charge carriers and reduced recombination rate.[20] Several binary and ternary metal oxide NCPs have been reported for their enhanced antibacterial and photocatalytic activity such as ZnO–NiO,[21] ZnO–CdO,[22] ZnO–MgO,[23] NiO–CeO_2–ZnO,[24] ZnO–CeO_2–TiO_2 [25] *etc.*, but there is still a need to develop more NCP materials having a more appropriate bandgap and easily excitable electrons to enhance photocatalytic efficiency.

The development of ternary metal oxide NCP using abundantly available salts is a viable method to develop cheap and effective NCP materials for improved photocatalytic applications. Many NPs can be utilized to synthesize ternary NCPs such as, ZnO is an n-type semiconductor having a wide band gap energy 3.32 eV and can also be easily used for biological applications due to its safe nature. NiO is p-type semiconductor having a wide band gap energy (3.5 eV) and have excellent electronic and magnetic properties. CuO is p-type semiconductor with having band gap energy 1.2 eV and high electrical conductivity and optical transmission in the visible region.[26–29] All the NPs of these metal oxides have exhibited antibacterial and photocatalytic properties. To enhance their properties, metal oxide NCPs are designed to be synthesized that may show better magnetic, structural, optical, catalytic, and thermal properties compared to individual components.[30,31]

In current work, we have investigated the impact of varying molar ratios of the Zn, Ni and Cu oxides on the structural, optical, morphological, dielectric, DC electrical, antibacterial, and photocatalytic properties of the NCP. We aimed to synthesize better photocatalytic materials for wastewater treatment. We have synthesized ternary metal oxide (ZnO–NiO–CuO) NCP with different molar ratios of metals (Zn : Ni : Cu) in NCPs *via* the hydrothermal method. All the NCPs have been evaluated for their photocatalytic potential for the degradation of hazardous dyes (MB, MO and mixture of both these dyes) under sunlight irradiation. Moreover, antibacterial potential of all these NCPs has also been evaluated against Gram-positive and Gram-negative bacterial strains.

2. Experimental procedure

2.1 Materials and instruments used

The raw materials used for synthesis were zinc chloride ($ZnCl_2$), nickel(II) nitrate hexahydrate ($Ni(NO_3)_2 \cdot 6H_2O$), copper(II) chloride dihydrate ($CuCl_2 \cdot 2H_2O$) and sodium hydroxide (NaOH). All

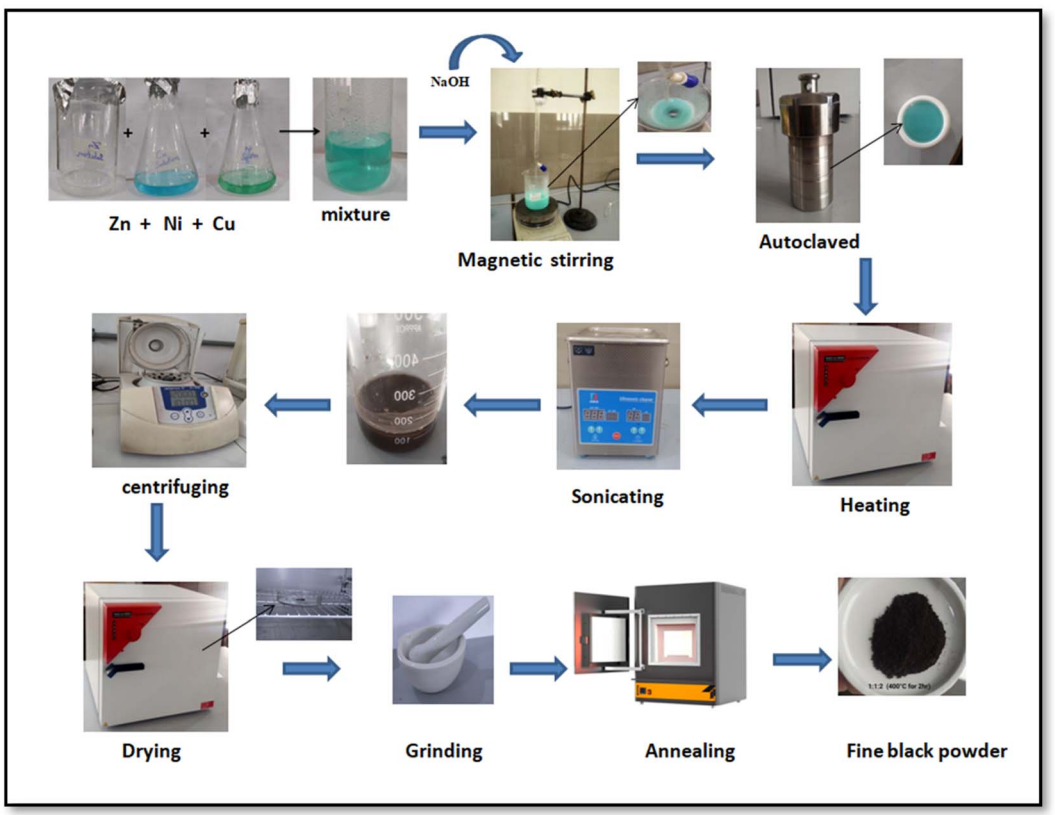

Fig. 1 General scheme of synthesis of ZnO–NiO–CuO NCPs.

the chemicals were purchased from Sigma Aldrich with purity >99%. All solutions were prepared in distilled water. Water and ethanol were used to wash the samples.

Powder XRD (PXRD) analysis was carried out by XRD (JDX-3532, JEOL, Japan) with Cu-Kα lines (wavelength 1.5418 Å). The XRD analysis was conducted with parameters set at a step duration of 0.04 seconds and utilizing a moderate scanning speed. SEM (JSM5910, JEOL, Japan) having maximum magnification and resolving power (3 000 00× and 2.3 nm) was used to capture the pictures of samples for morphological analysis of samples. The SEM analysis was conducted at an electric current of 106 mA, a working distance of 9.03 mm, and by employing non-metallization process. The UV-visible spectrophotometer (Shimadzu Japan, Pharmaspec-1700) was used to record the absorbance spectra in the range of 200 to 800 nm. The thermal analysis (TGA/DSC) was performed with Discovery 650 SDT thermal analyzer (TA instruments, USA) from 25 to 1000 °C. The heating rate was maintained at 20 °C min^{-1} using ultra-pure (99.99%) N_2 gas at flow rate of 50 mL min^{-1}. LCR meter, Keithley *I–V* measurement (model 2100) was used to measure electrical properties of samples.

2.2 Synthesis of NCPs

To prepare ZnO–NiO–CuO (1 : 1 : 1) NCPs, 50 mL of 0.1 M solution of each precursor salt was prepared by dissolving 0.68 g, 1.45 g and 0.85 g of anhydrous $ZnCl_2$, $Ni(NO_3)_2 \cdot 6H_2O$ and $CuCl_2 \cdot 2H_2O$, respectively in distilled water. These solutions were then mixed with constantly stirring for 30 minutes at room temperature. 50 mL of 1 M solution of NaOH was also prepared and added in the above solution of salts until the pH 10 was maintained. The resulting solution was stirred for one hour at 50 °C. The resulting dark green colored solution was poured into a Teflon lined autoclave, heated at 150 °C for 12 hours, and then cooled to room temperature. The black precipitates obtained were collected and sonicated. The precipitates were washed thrice with distilled water and ethanol and mixture was centrifuged at 13 000 rpm for 10 minutes after each washing. Subsequently, the sample was dried at 80 °C in the oven for 3 hours and then grinded by mortar and pestle into fine black powder. This powder was annealed at 400 °C for 2 hours as reported in literature.[32] To synthesize the ZnO–NiO–CuO NCPs with different molar ratios (2 : 1 : 1, 1 : 2 : 1 and 1 : 1 : 2), the same procedure was performed using the desired precursor salt ratios (Fig. 1).

2.3 Photocatalytic degradation of dyes

The photocatalytic efficiency of the ZnO–NiO–CuO NCPs was determined by degradation of MB, MO and mixture of dyes (MB + MO) solution under sunlight irradiation following the procedure reported in literature.[10,33] Briefly, 10 ppm solution of MB and MO dyes were prepared in distilled water, separately. 10 mg of the each ZnO–NiO–CuO NCPs powder was added separately in each 100 mL aliquot of dyes and stirred for 30 minutes in dark to maintain adsorption–desorption equilibrium. Subsequently, each mixture was exposed to sunlight and spectra were recorded at 668 nm for MB and 464 nm for MO after every 15 minutes till 90 minutes exposure. With the passage of time, the color of the dye solutions (MB and MO) started to diminish, indicating the degradation of the dyes. The absorbance data was used to determine the % degradation of dyes after regular intervals following the eqn (1).

$$\%\ \text{degradation of dye} = \frac{C_0 - C_t}{C_0} \times 100\% \quad (1)$$

where C_o and C_t represent the initial concentration of the dye (before irradiation) and final concentration of dye after each regular interval.

2.4 Antibacterial activity

The antibacterial activity of ZnO–NiO–CuO NCPs was evaluated following the disc diffusion method.[32,34–36] Two Gram-positive strains (*S. aureus* and *B. subtilis*) and two Gram-negative strains (*E. coli* and *P. aeruginosa*) of bacteria were used for this study. The bacterial strains were grown in nutritional agar for 24 hours at 4 °C, and the turbidity of the cultures was controlled with saline solution (0.9% NaCl) and maintained at 108 CFU (colony forming unit). Fresh nutrient agar (3 g/100 mL) was seeded with the already prepared inoculum after autoclave at 45 °C at pH 7.25 mL of each seeded agar was placed in Petri dish plate. Sterile paper discs loaded with pure DMSO and solutions of NCPs in DMSO (2 mg mL^{-1}) were placed in Petri dishes. These Petri dishes were kept in incubator at 37 °C for next 24 h. After 24 h, the inhibition zone of inhibitions of each NCP were measured in millimeters using a Vernier caliper to evaluate the antibacterial activity.

2.5 Statistical analysis

Triplicate analysis was carried out for each photocatalytic and antibacterial test. The results were analyzed statistically by ANOVA. Statistical significance was accepted at a level of $p < 0.05$. All the results were reported as mean ± SD.

3. Results and discussion

3.1 XRD analysis

The XRD patterns of ZnO–NiO–CuO NCPs with different molar ratio of metals (Zn : Ni : Cu) 1 : 1 : 1, 2 : 1 : 1, 1 : 2 : 1, and 1 : 1 : 2 annealed at 400 °C, labeled as ZNC (1 : 1 : 1), ZNC (2 : 1 : 1), ZNC (1 : 2 : 1), and ZNC (1 : 1 : 2), respectively, are shown in Fig. 2. The XRD peaks of samples were matched with the library of XRD patterns which confirmed the hexagonal Wurtzite structure of ZnO (COD No. "9004180"),[29] the cubic structure of NiO (COD No. "01-089-3080")[31] and the monoclinic structure of CuO (COD No. "9016105").[29] The XRD peaks showed the presence of three phases in a single matrix. The ZnO peaks were found at diffraction angles of 2θ = 31.7°, 34.5°, 36.2°, 47.6°, 56.7°, 62.6°, 66.3°, 67.9°, 69.1° corresponding to Miller indices (100), (002), (101), (102), (110), (103), (200), (112), and (201), respectively. The NiO peaks appeared at diffraction angles of 2θ = 37.1°, 43.1°, 62.6°, 75.1°, 79.0° corresponding to Miller indices (111), (200), (220), (311), and (222), respectively and the CuO peaks at 2θ = 31.8°, 35.5°, 38.8°, 47.5°, and 66.3° corresponding to Miller indices (110), (111), (200), (−202), and (022), respectively. The XRD patterns exhibited no ambiguous peaks, confirming the

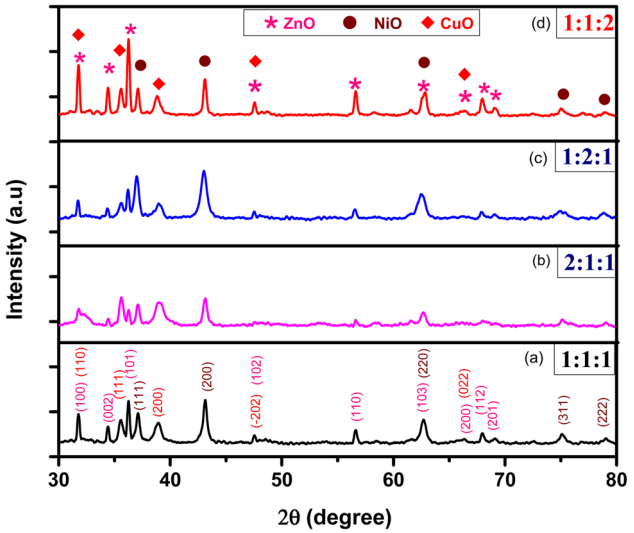

Fig. 2 XRD patterns of NCPs for different molar ratios of ZnO : NiO : CuO; (a) 1 : 1 : 1 (b) 2 : 1 : 1 (c) 1 : 2 : 1 (d) 1 : 1 : 2.

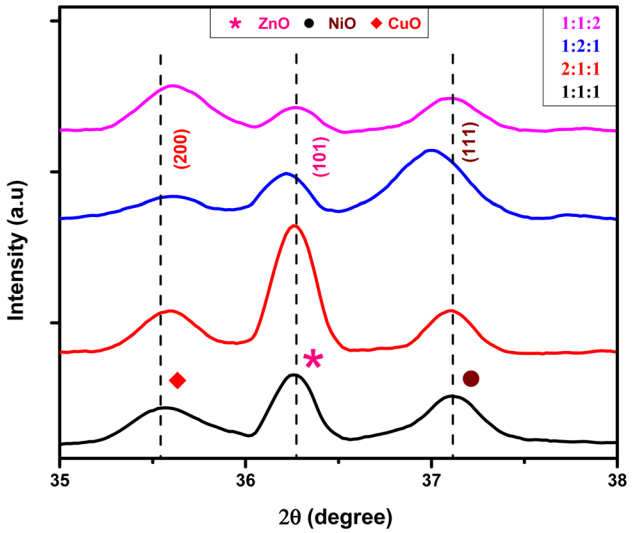

Fig. 3 Shifting of peaks in samples with different molar ratios.

Table 1 Lattice parameters of samples with different molar ratios

Samples	Oxides	a (A°)	b (A°)	c (A°)	c/a	V (A°)^3	d-Spacing (A°)
ZNC-(1 : 1 : 1)	ZnO	3.24	3.24	5.19	1.60	47.40	1.8950
	NiO	4.19	4.19	4.19	1.00	73.77	1.6911
	CuO	4.63	3.39	5.03	1.08	78.28	2.1131
ZNC-(2 : 1 : 1)	ZnO	3.24	3.24	5.20	1.60	47.56	1.8946
	NiO	4.19	4.19	4.19	1.00	73.77	1.6923
	CuO	4.63	3.40	4.99	1.07	77.72	2.1119
ZNC-(1 : 2 : 1)	ZnO	3.25	3.25	5.21	1.60	47.73	1.8921
	NiO	4.20	4.20	4.20	1.00	74.56	1.6984
	CuO	4.62	3.43	4.93	0.93	77.32	2.1144
ZNC-(1 : 1 : 2)	ZnO	3.25	3.25	5.20	1.60	47.61	1.8951
	NiO	4.19	4.19	4.19	1.00	73.92	1.6944
	CuO	4.62	3.42	4.90	0.94	76.66	2.1120

purity and high crystallinity of NCPs. The appearance of three phases due to ZnO, NiO and CuO in the samples, confirmed the successful synthesis of a ternary metal oxide ZnO–NiO–CuO NCPs.

The lattice constants (a, b, and c) and unit cell volume (V) for cubic NiO, hexagonal ZnO, and monoclinic CuO were measured using the eqn (2)–(4) following the literature.[30]

$$\frac{1}{d^2} = \frac{h^2 + k^2 + l^2}{a^2} \text{ and } V = a^3 (\text{for cubic}) \quad (2)$$

$$\frac{1}{d^2} = \frac{4}{3}\left(\frac{h^2 + hk + k^2}{a^2}\right) + \frac{l^2}{c^2} \text{and } V = 0.866\left(a^2 c\right)(\text{for hexagonal}) \quad (3)$$

$$\frac{1}{d^2} = \frac{1}{\sin^2 \beta}\left(\frac{h^2}{a^2} + \frac{k^2 \sin^2 \beta}{b^2} + \frac{l^2}{c^2} - \frac{2hk \cos \beta}{ab}\right) \text{and } V = abc \sin \beta (\text{for monoclinic}) \quad (4)$$

where 'd' is the interplanar spacing measured using Bragg"s law, and 'h', 'k', and 'l' are the Miller indices mentioned in Table 1.

The presence of Zn, Ni, and Cu with their distinct ionic radii (0.74 Å, 0.69 Å, and 0.73 Å for Zn^{2+}, Ni^{2+}, and Cu^{2+}, respectively) in NCPs caused slight shifts in the metal oxide peaks as shown in Fig. 3. The XRD peaks of metal oxides were shifted in synthesized NCPs compared to pure metal oxide NPs in consistent with the literature.[37,38] This may happen due to mutual interactions of metal oxides, resulting in new phases with unique lattice parameters and crystal structures.

3.1.1 Relative intensity ratios. The relative intensity ratios corresponding to the volume fractions of ZnO, NiO, and CuO in the synthesized samples can be estimated by the following relations presented in eqn (5)–(7).[30]

$$R_{ZnO} = \frac{I_{ZnO}}{I_{ZnO} + I_{NiO} + I_{CuO}} \quad (5)$$

Table 2 Relative intensity ratios% of samples with different molar ratios

Sample	Oxides	Peaks	Peak intensity	Relative intensity ratios%
ZNC-(1 : 1 : 1)	ZnO	(101)	41.98	39.62
	NiO	(200)	40.71	38.42
	CuO	(111)	23.27	21.96
ZNC-(2 : 1 : 1)	ZnO	(101)	96.22	58.99
	NiO	(200)	39.90	24.46
	CuO	(111)	26.99	16.55
ZNC-(1 : 2 : 1)	ZnO	(101)	33.02	34.27
	NiO	(200)	48.35	50.17
	CuO	(111)	14.99	15.56
ZNC-(1 : 1 : 2)	ZnO	(101)	37.83	28.19
	NiO	(200)	47.67	35.53
	CuO	(111)	48.65	36.26

Table 3 Parameters of NCPs for different molar ratios

Samples	Oxides	Average crystalline size D (nm) Scherer method	W–H plot method	Dislocation density $\delta \times 10^{-3}$	Lattice strain $\varepsilon \times 10^{-3}$
ZNC-(1 : 1 : 1)		21.51	18.88	3.13	0.91
	ZnO	26.54	58.99	1.78	0.76
	NiO	16.42	15.51	3.77	1.2
	CuO	18.23	15.99	4.83	0.78
ZNC-(2 : 1 : 1)		27.91	33.16	1.84	0.72
	ZnO	32.63	353.83	1.25	0.66
	NiO	24.05	47.79	1.92	0.96
	CuO	24.91	18.93	2.93	0.60
ZNC-(1 : 2 : 1)		23.03	42.78	4.38	1.11
	ZnO	31.76	110.88	2.06	0.78
	NiO	12.41	35.81	7.30	1.90
	CuO	21.83	15.10	5.16	0.78
ZNC-(1 : 1 : 2)		20.23	15.77	7.04	1.28
	ZnO	22.39	18.49	8.90	1.47
	NiO	19.48	27.45	2.71	1.13
	CuO	11.43	10.86	12.97	1.23

$$R_{NiO} = \frac{I_{NiO}}{I_{ZnO} + I_{NiO} + I_{CuO}} \quad (6)$$

$$R_{CuO} = \frac{I_{CuO}}{I_{ZnO} + I_{NiO} + I_{CuO}} \quad (7)$$

The calculated relative intensity ratios corresponding to the volume fractions of NiO, ZnO, and CuO in the synthesized samples are given in Table 2.

3.1.2 Debye Scherrer method. The crystalline sizes of the NCPs were determined using Debye Scherrer the formula as shown by eqn (8).[39]

$$D = \frac{K\lambda}{\beta_D \cos\theta} \quad (8)$$

where D is crystalline size, λ is X-ray wavelength, θ is diffraction angle, β is FWHM, and K is Shape factor (typically 0.9). The dislocation density (δ) was measured using standard relation

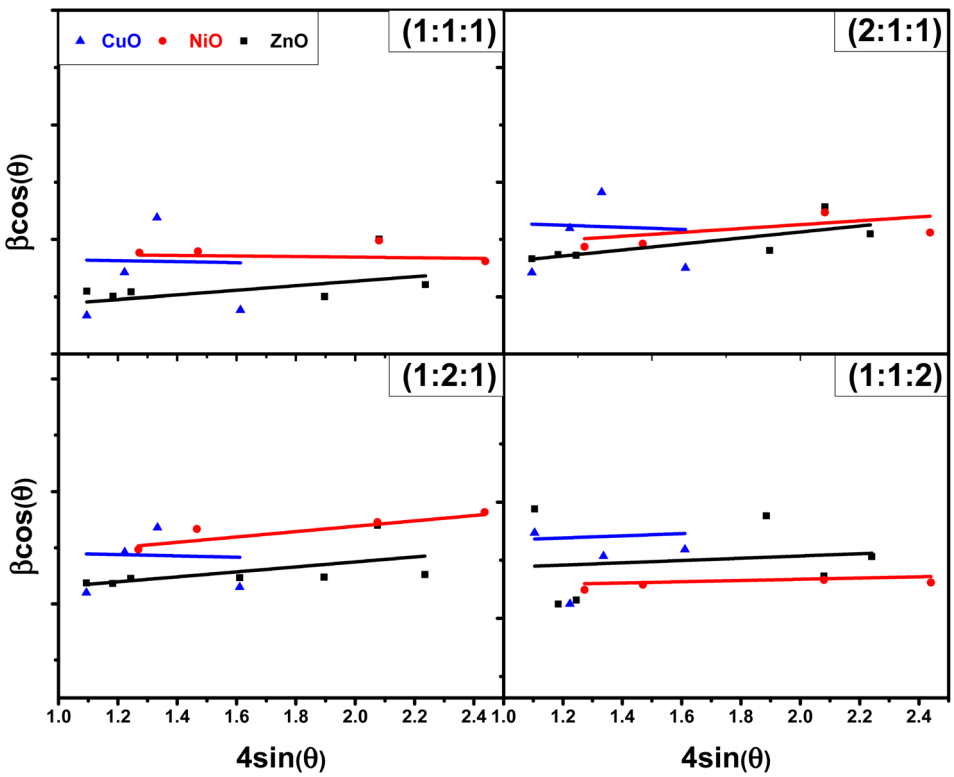

Fig. 4 Plots of W–H method for NCPs with different molar ratios.

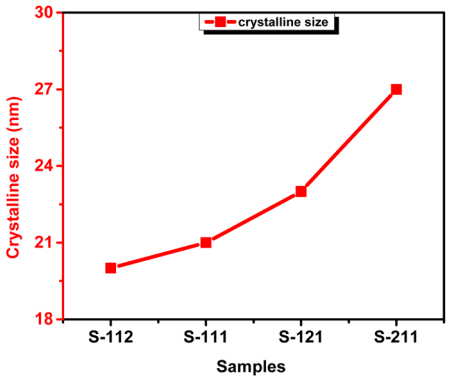

Fig. 5 Variation in crystalline size with samples.

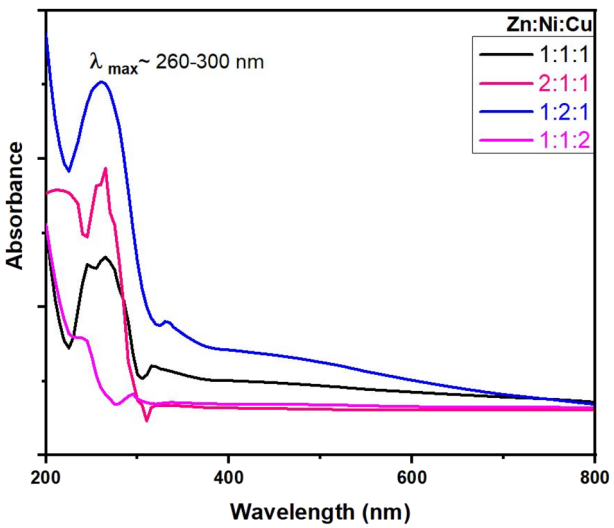

Fig. 6 UV-vis spectra of NCPs with different molar ratios.

$\left(\delta = \frac{1}{D^2}\right)$. The calculated crystalline size, micro strain, and dislocation density are given in Table 3.

3.1.3 Williamson–Hall (W–H) plot method. Williamson–Hall (W–H) method is another way to find the crystalline size of NPs. It is based on finding the broadening of diffraction peaks in the XRD pattern caused by crystallite size and micro strain (ε).[17] The total peak broadening relation is presented in eqn (9).

$$\beta_{hkl} \cos\theta = \frac{K\lambda}{D} + 4\varepsilon \sin\theta \quad (9)$$

The W–H method involves plotting $4 \sin\theta$ and $\beta hkl \cos\theta$ (shown in Fig. 4) to determine crystalline size and micro strain, with the slope representing micro strain and the intercept indicating crystallite size. A comparison between the results obtained using the Scherrer method and the W–H plot method is provided in Table 3, showing the different contributions of crystallite size and strain to peak broadening.

The XRD analysis revealed that by increasing the molar ratios (ZNC-(2 : 1 : 1 and 1 : 2 : 1)), except for the increasing molar ratio of Cu (ZNC-(1 : 1 : 2)), resulted in larger crystallite sizes compared to the sample (1 : 1 : 1) having equal molar concentration of all the metals. When the molar ratio of metals is increased, it promotes the availability of additional ions that act as nucleation sites, resulted in facilitating the formation of new crystal nuclei. This enhanced nucleation leads to the growth of larger crystallites as shown in Fig. 5. The highest crystalline size was observed in the sample ZNC-(2 : 1 : 1). This can be attributed to the role of Zn ions in enhancing the diffusion rates of the metal ions during the synthesis process, thereby promoting the growth of crystallites in the sample. Consequently, the growth of ZnO crystallites was favored over that of NiO and CuO when the molar ratio of Zn was increased. In contrast, the sample ZNC-1 : 1 : 2 exhibited the smallest crystalline size. This can be attributed to the different growth kinetics of Cu ions compared to Zn and Ni ions, which disrupt the crystalline growth process and hinders the formation of larger crystallites.[40,41]

3.2 UV-vis spectral analysis

Fig. 6 shows the UV-vis absorption spectra obtained for ZnO–NiO– CuO NCPs within the 200–800 nm range. The absorption maxima (λ_{max}) are observed in the range of 230 to 330 nm. These λ_{max} values align closely with the literature values ZnO,[42] NiO,[43] CuO–ZnO–NiO,[32] ZnO–NiO,[44] ZnO–CuO,[45] and NiO–CuO,[46] verifying the successful production of the NCPs. The NCPs exhibit lower absorption maxima compared to pure ZnO, CuO, and NiO NPs. This decrease in the absorption maxima is due to either the coupling of metal oxides or the formation of defect energy levels within the NCP.[44,47] The absorption coefficient (α) was derived using the eqn (10).[27]

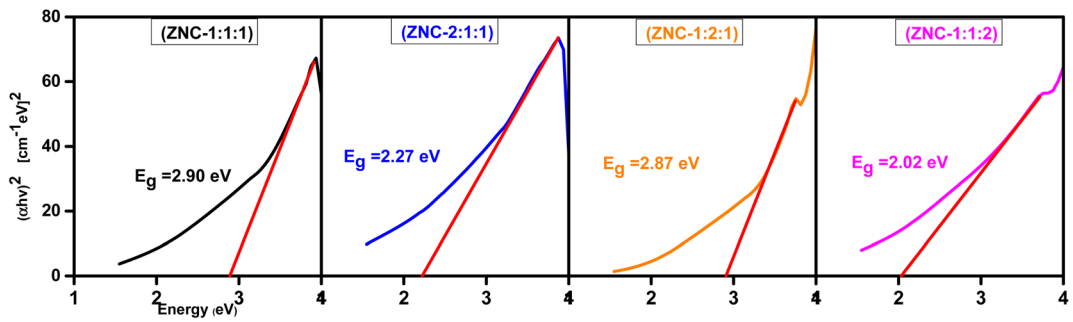

Fig. 7 Tauc plots of NCPs for determination of bandgap energies.

Table 4 Bandgap values of NCPs calculated by Tauc plots

Sample	λ_{max} (nm)	E_g (eV)
ZNC-(1 : 1 : 1)	263	2.90
ZNC-(2 : 1 : 1)	265	2.27
ZNC-(1 : 2 : 1)	259	2.87
ZNC-(1 : 1 : 2)	293	2.02

$$\alpha = \frac{2.303A}{t} \quad (10)$$

Here; A and t represents the absorbance and thickness of the cuvette, respectively.

The optical bandgap (E_g) was determined using the relation shown in eqn (11).

$$\alpha h\nu = A(h\nu - E_g)^{\gamma} \quad (11)$$

where, "$h\nu$" represents the photon energy, "A" denotes a constant, and "E_g" corresponds to the bandgap energy. The parameter "γ" in the equation, known as the Tauc exponent, for direct bandgap materials, γ has a value of 1/2, while for indirect bandgap materials; γ takes a value of 2.[48] To find the direct bandgap (E_g), a plot of $(\alpha h\nu)^2$ against $h\nu$ was generated as shown in Fig. 7, and bandgap values of each NCPs were obtained as given in Table 4.

The effect of molar ratios on the NCPs can be observed from Fig. 6. The absorption peaks were shifted and distinct bandgap values (Fig. 7) were obtained by changing the molar ratios of components of NCP. The observed behavior of the samples can be understood by considering the individual properties of each metal oxide and their interactions within the NCP. All components (metal oxides) of NCP exhibits different bandgap such as NiO has 3.6–4.0 eV, ZnO has ~3.37 eV and CuO has a smaller bandgap of 1.2 eV.[26] These differences in bandgap values influence the overall bandgap behavior of the NCP as the molar concentrations of the metal oxides vary. When increasing the molar concentration of NiO in the NCP, the larger bandgap of NiO (ZNC-(1 : 2 : 1)) dominates and contributes to an overall larger bandgap in the NCP. ZnO has a smaller bandgap compared to NiO but is larger than CuO so the sample with an increased molar ratio ZnO (ZNC-211) exhibits an intermediate bandgap compared to the other two. When increasing the molar concentration of CuO in the NCP (ZNC-(1 : 1 : 2)), the smallest bandgap of CuO dominates and becomes the major contributor to the overall bandgap.[49] The specific properties and electronic structures of each metal oxide determine the overall bandgap of the composite material when their molar concentrations are modified.[50]

3.3 FTIR analysis

FTIR analysis is performed to confirm the presence of major functional groups present in the samples. The FTIR spectrum of the CuO–NiO–ZnO NCPs is displayed in Fig. 8. The FTIR spectra showed the presence of broad peaks in the region of 3250–3600 cm^{-1} due to hydroxyl groups attached to the NCPs surface. Narrow peaks present in the region of 450–1000 cm^{-1} were assigned to the M–O bonds. Peaks in the region of 800–930 cm^{-1}, 600–750 cm^{-1} and 450–570 cm^{-1} were assigned to the Zn–O, Ni–O and Cu–O bonds, respectively.[51,52] It was also observed that the relative absorption of selective bond peak was empirically increased with increase of molar ratio that particular metal in NCPs.

3.4 SEM and EDX analysis

SEM analysis of NCPs was performed to observe the morphology of samples. SEM images of the CuO–NiO–ZnO NCPs are shown in Fig. S1.† The micrographs of ZNC-(1 : 1 : 1) [Fig. S1a†], ZNC-(2 : 1 : 1) [Fig. S1b†], ZNC-(1 : 2 : 1) [Fig. S1c†] and ZNC-(1 : 1 : 2) [Fig. S1d†] revealed the presence of irregular (rough) mixed rod

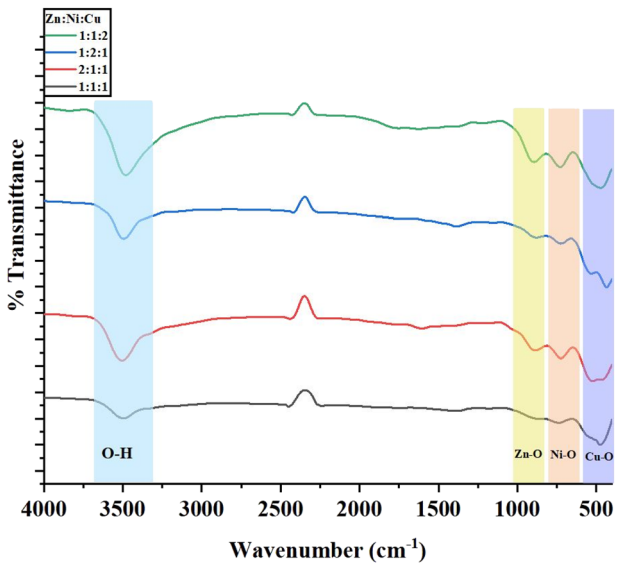

Fig. 8 FTIR spectra of NCPs with different molar ratios.

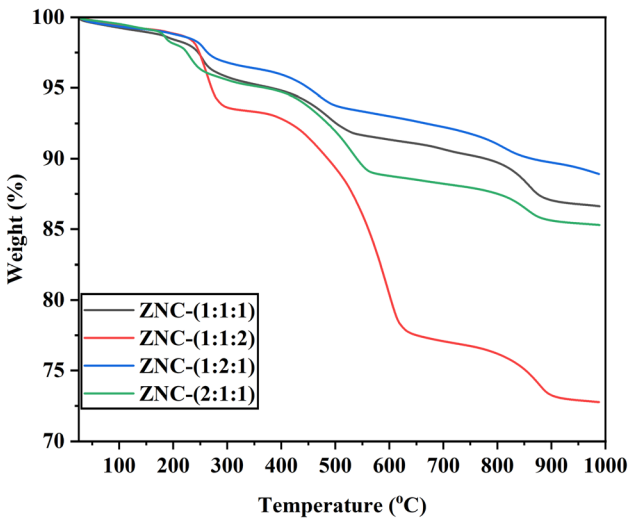

Fig. 9 Thermogram of ternary metal oxide NCPs.

Table 5 Thermogravimetric analysis of ternary metal oxide NCPs

	Weight loss (%) at different temperatures								
Nanocomposite	373 K	473 K	573 K	673 K	773 K	873 K	973 K	1073 K	1173 K
ZNC-(1 : 1 : 1)	0.88	1.51	4.3	5.13	7.41	8.64	9.36	10.32	12.98
ZNC-(1 : 1 : 2)	0.68	1.06	6.43	7.19	10.56	19.54	22.93	23.81	26.82
ZNC-(1 : 2 : 1)	0.76	1.12	3.32	4.05	6.22	7.00	7.76	8.95	10.32
ZNC-(2 : 1 : 1)	0.52	1.81	4.53	5.29	8.05	11.24	11.79	12.53	14.37

and spherical highly agglomerated structures. It proved the good compatibility between the different metal oxides phases present within the NCPs.

EDX analysis of the samples synthesized at different concentration ratios was carried out to check the purity and compositional analysis as shown in Fig. S2–S4.† The elemental analysis showed the peaks of all the elements (Zn, Cu, Ni and O) in the EDX spectra with strong agreement to the ratio of salts used for each ternary metal oxide. The absence any other peaks due to impurities also proved the purity of samples.

3.5 Thermal analysis

Thermogravimetric analysis (TGA) of all the NCPs was carried out in the temperature range of 25–1000 °C at constant heating rate of 20 °C under nitrogen atmosphere. TGA data of all the ternary metal oxide composites was found in good concurrence with the configuration and putrefaction process under heating conditions. All the NCPs were found highly stable in the range of 25–1000 °C with minimum weight loss (%). The thermograms of all the NCPs are shown in Fig. 9 and weight loss (%) of each composite at various temperatures is depicted in Table 5.

From thermograms, it can be observed that all the NCPs were decomposed in at least three stages and maximum weight loss (26.82%) was exhibited by the ZNC-(1 : 1 : 2), which was due to pyrolysis of CuO at high temperature. All the NCPs have shown minimum weight loss (~7%) up to 400 °C. This weight loss was attributed to the loss of water molecules attached at the surface of NCPs. Weight loss observed in the range of 400–600 °C was might be due to elimination of coordinated water molecules.[53] In third stage of decomposition (above 800 °C), weight loss was observed due to break down of Cu–O bond and resulting pyrolysis of nanocomposites.[54]

3.6 DC electrical properties

From the slope of the current–voltage (I–V) graph, we can measure the resistance $\left(R = \frac{1}{\text{slope}}\right)$, resistivity $\left(\rho = \frac{RA}{l}\right)$ and conductivity $\left(\sigma = \frac{1}{\rho}\right)$ of NCPs. The temperature-dependent electrical conductivity and resistivity behavior was observed in all synthesized NCPs, indicating the expected semiconducting behavior as shown in Fig. 10a and b. In the temperature range of 400–700 K, the conductivity of the NCPs increased as the temperature was increased.[55,56] In semiconducting materials, as the temperature rises above 400 K, the thermal energy increases, resulting in the promotion of charge carriers from the VB to the CB. This process increases the number of charge carriers available for conduction, thus enhancing electrical conductivity. It was observed that higher molar concentrations resulted in a greater density of charge carriers within the NCP, which has further enhanced the conductivity.[57,58]

To calculate the activation energy using resistivity measurements, we employed the Arrhenius relation, represented in eqn (12).

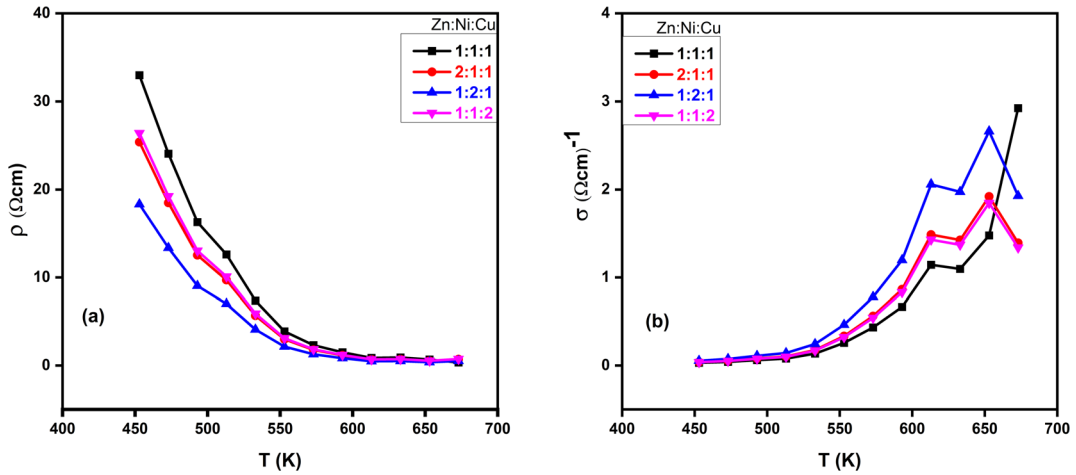

Fig. 10 Temperature-dependant (a) resistivity and (b) conductivity of ZnO–NiO–CuO NCPs at different molar concentrations of metals.

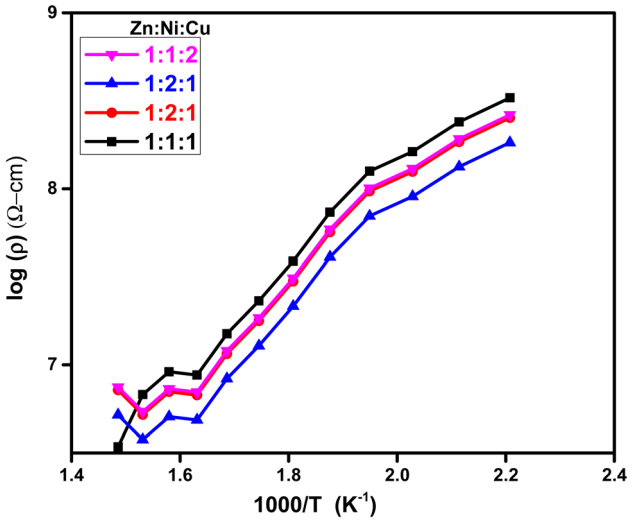

Fig. 11 Plot of log(ρ) *vs.* 1000/T at different molar ratios.

$$\rho = \rho_{\infty} \exp\left(\frac{E_a}{K_\beta T}\right) \quad (12)$$

This eqn (12) relates the temperature-dependent resistivity (ρ) to the activation energy (E_a).[59] From Fig. 11, It was observed that as the molar concentration of the metal oxide increases, there is a decrease in activation energy due to an increase in the availability of charge carriers (electrons or holes) within the NCP. Nanomaterials with high electrical conductivity can be used in high-speed electronics, sensors, and energy generation and storage devices.

3.7 Dielectric properties

The dielectric analysis of the synthesized samples indicated that ε_r, ε_i, dielectric loss (tan δ), and impedance (Z) demonstrate higher values at lower frequencies of the applied electric field, as depicted in Fig. 12 and 13. As the frequency increases, these values gradually decrease. At low frequencies, high dielectric constant values were observed due to oxygen vacancies present in the lattice, defects at the grain boundaries, and low conductivity at the grain boundaries. The observed dielectric behavior in metal oxide NCPs can be explained more thoroughly by combining the Maxwell–Wagner interfacial model and Koop's phenomenological hypothesis,[60] which takes into account the roles of both conducting grains and interfaces in determining the dielectric properties. According to the model, the material is considered a composite of conducting grains and interfaces or grain boundaries. Due to the influence of an external electric field, charge carriers in conducting grains exhibit enhanced mobility, while accumulation occurs at the interfaces or grain boundaries due to their resistive properties. This accumulation results in significant polarization and results in a high dielectric constant in the material.[61,62] These interfaces often have higher resistance or lower conductivity, so the flow of charge carriers is impeded within the material, leading to higher impedance and dielectric loss.[63] As the frequency increases, the grain boundaries become less significant due to ionic displacement lag. As the frequency of the applied electric field increases, the ionic displacement within the material lags behind the rapid changes in the field.[64] This reduces the resistance and impedance, leading to a decrease in dielectric loss and dielectric constant as shown in Fig. 12(a) and (b).

As the molar concentration increases, there is a corresponding rise in the dielectric constant of metal ions in the ZnO–NiO–CuO NCPs due to the increased polarization response resulting from a higher density of charge carriers within the material. The observed increase in dielectric constants is due to the higher density of charge carriers within the grains.[61] Each metal ion contributes differently to the dielectric response of the NCP due to its unique electronic structure and polarizability. The

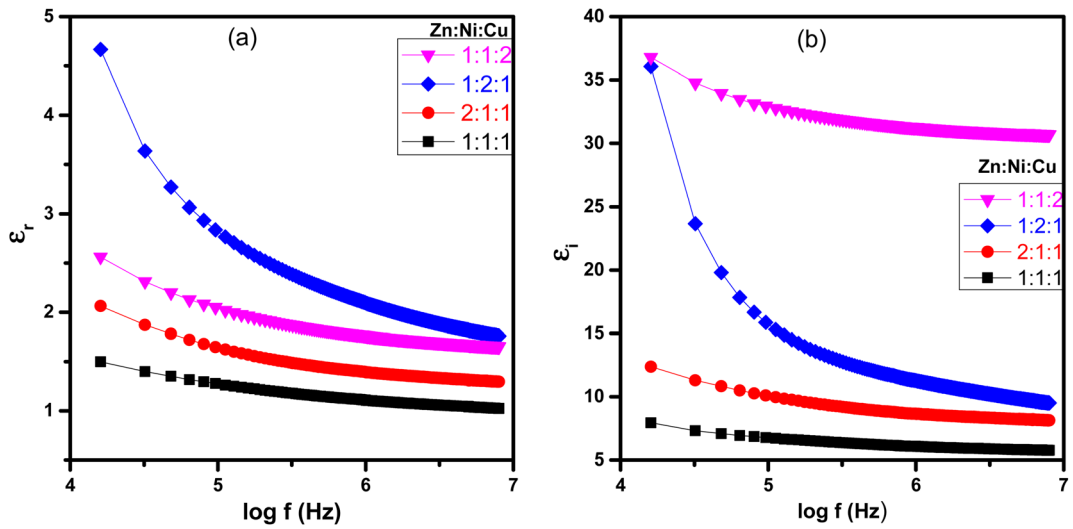

Fig. 12 Plots of NCPs with different molar ratios (a) log(f) *vs.* ε_r and (b) log(f) *vs.* ε_i.

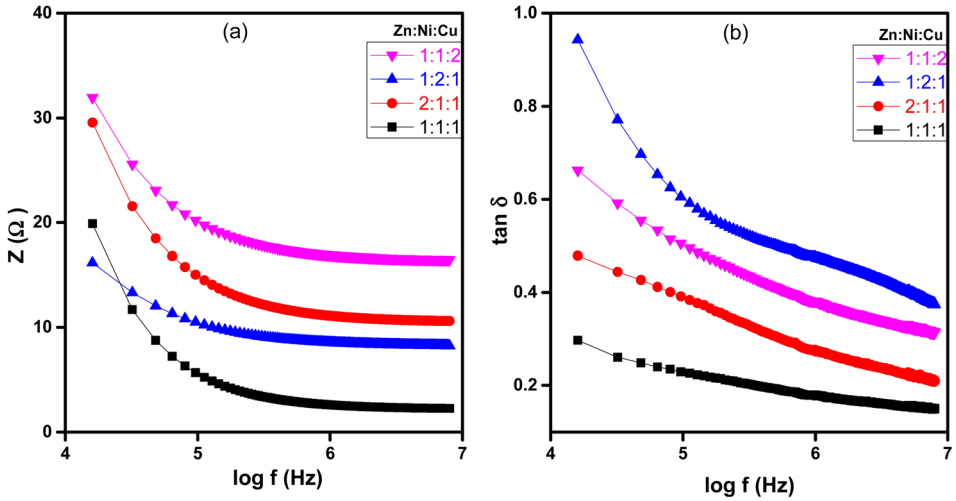

Fig. 13 Plots of NCPs with different molar ratios (a) log(*f*) *vs.* impedance (*z*), and (b) log(*f*) *vs.* dielectric loss (tan *δ*).

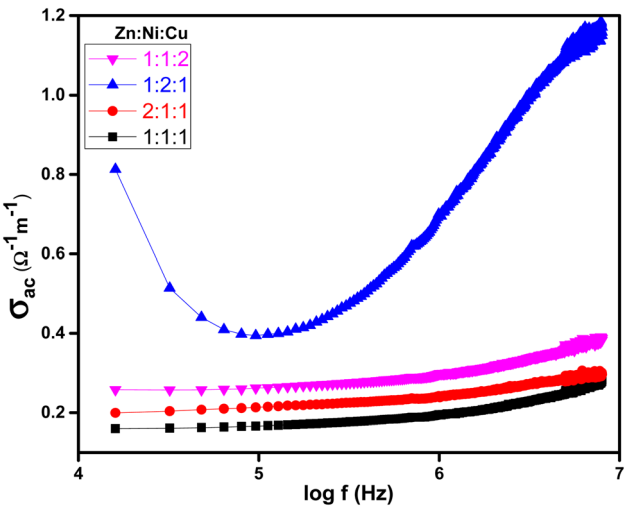

Fig. 14 Plot of log(*f*) *vs.* σ_{ac} at different molar ratios of ZnO–NiO–CuO NCPs.

dielectric constant is influenced by factors such as the charge, size, and electronic configuration of the metal ions.

Fig. 13(a) and (b) showed that impedance (*Z*) and dielectric loss (tan *δ*) of the ZnO–NiO–CuO NCPs increased by increasing the molar concentration of different metals in the NCP. As discussed earlier, the increased molar concentration results in an increase in the dielectric constant value of the synthesized NCPs, which contributes to enhanced polarization effects, increased resistivity, and greater mobility of charge carriers within the material. These factors collectively contribute to the observed increase in both the dielectric loss and impedance.

3.8 AC electrical conductivity

Fig. 14 shows the relationship between AC conductivity (σ_{ac}) and the applied electrical frequency of synthesized samples. The increase in AC conductivity of ZnO–NiO–CuO NCPs was observed with increasing frequency, as depicted in Fig. 14. The increase in conductivity is due to the activation of a hopping mechanism as the electric field is applied.[65] The AC conductivity in a material is primarily attributed to the presence of mobile charge carriers. At low frequencies, the charge transfer is primarily limited to the nearest neighboring lattices.[66] When an electric field frequency increases, it provides the necessary energy for charge carriers to overcome these barriers and hop between these localized states or defect sites. This hopping process facilitates the movement of charge carriers and leads to an enhancement in conductivity.

Higher molar concentrations lead to an increase of charge carriers and also improve the mobility of charge carriers within the material. It also affects interfacial phenomena, such as inter-particle interactions and charge carrier hopping between localized states or defect sites. The different behavior observed when increasing the molar concentration of different metals (Zn, Ni, Cu) in the ZnO–NiO–CuO NCP (Zn : Ni : Cu 2 : 1 : 1, 1 : 2 : 1 and 1 : 1 : 2), was due to the distinct electronic, dielectric, morphological, and structural characteristics of each metal. These unique properties influence the AC conductivity of the NCP. Specifically, Ni possesses properties that promote higher conductivity compared to Zn and Cu. From Fig. 14, It was confirmed that the NCP sample with an increased concentration of Ni ions ZNC-(1 : 2 : 1) exhibited the highest AC conductivity.

4. Applications of ZnO–NiO–CuO NCPs

4.1 Photocatalytic efficacy of NCPs for dye degradation

Photocatalytic efficiency of each NCP was evaluated for the photodegradation of MB, MO and mixture of MB and MO dyes in the batch experiments. Decrease in color intensity and resulting absorbance decrease data was utilized to determine the % dye degradation after regular intervals. For further insight of the degradation kinetics, the rate constant of each experiment was determined using the eqn (13). All the

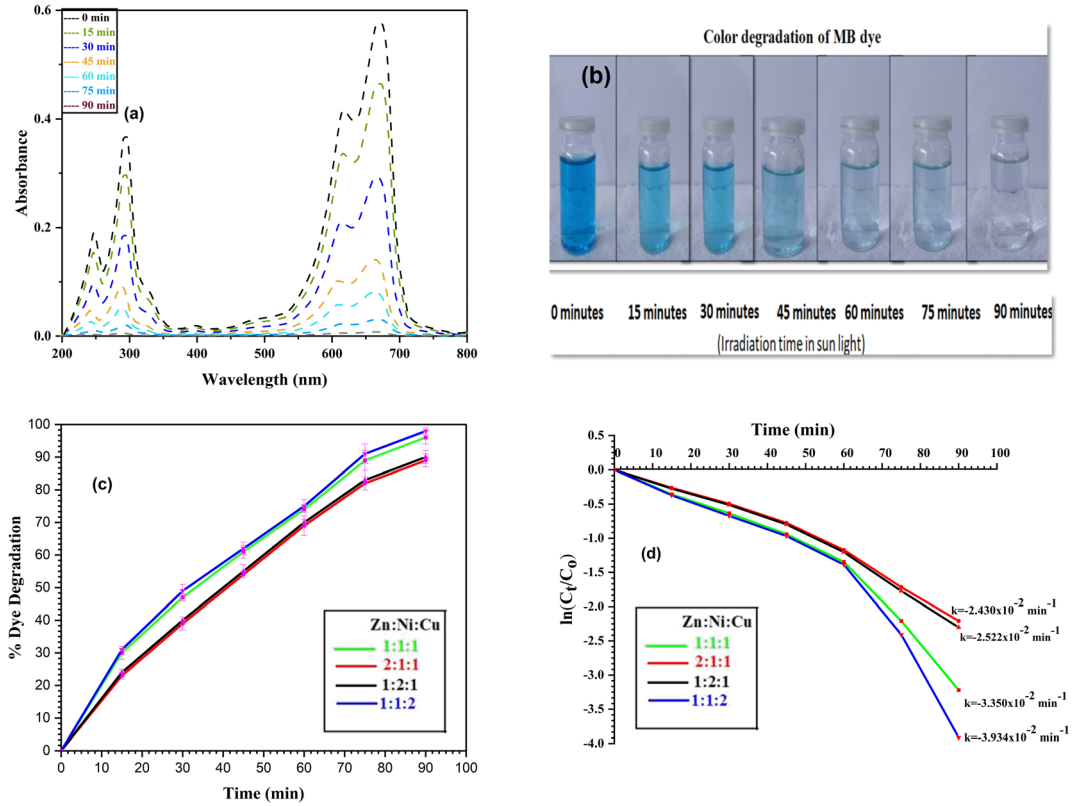

Fig. 15 MB dye degradation after regular intervals (a) absorbance spectra, (b) color degradation, (c) % dye degradation and (d) rate constant plot.

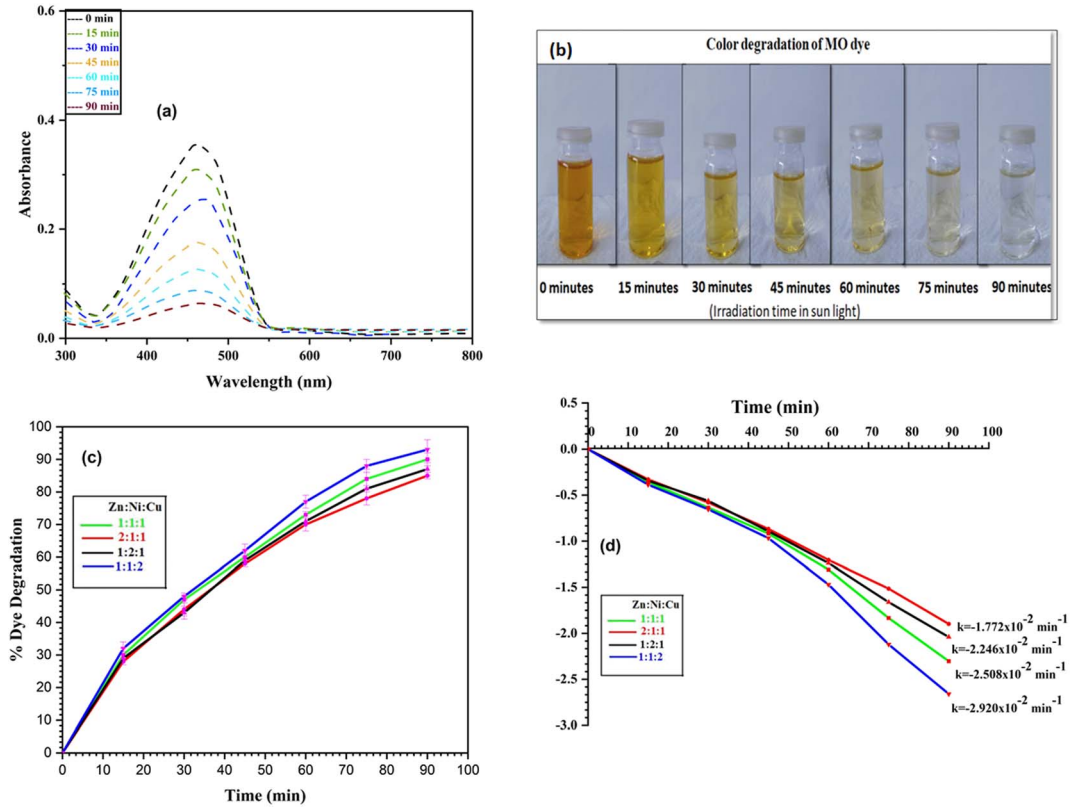

Fig. 16 MO dye degradation after regular intervals (a) absorbance spectra, (b) color degradation, (c) % dye degradation and (d) rate constant plot.

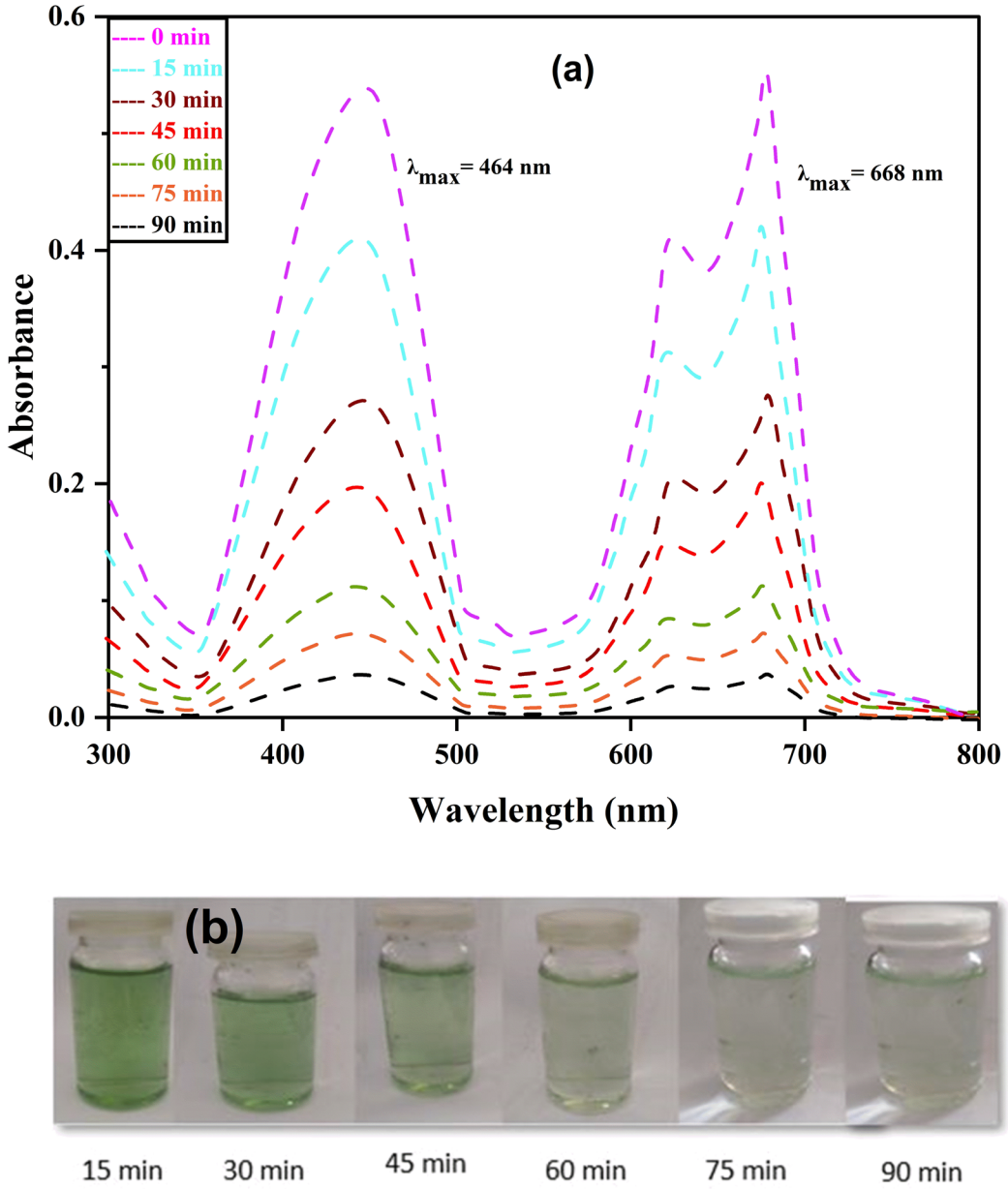

Fig. 17 Degradation of mixture of dyes after regular intervals (a) absorbance spectra; (b) change in color intensity.

photodegradation experiments followed the pseudo-first-order kinetics in consistent with the literature.[8]

$$\ln\left(\frac{C_t}{C_0}\right) = kt \quad (13)$$

Here 'k' represents the rate constant and is determined by examining the slope of the $\ln(C_0/C_t)$ *versus* irradiation time (t) plot.

4.1.1 Photodegradation of MB dye. The photodegradation of MB dye was performed under sunlight exposure using all the NCPs in batch experiments. Sharp decrease in the absorbance spectra ($\lambda_{max} = 668$ nm) (Fig. 15a) and color intensity (Fig. 15b) were observed for each NCP catalyst. ZNC-(1 : 1 : 1), ZNC-(2 : 1 : 1), ZNC-(1 : 2 : 1) and ZNC-(1 : 1 : 2) exhibited 96%, 89%, 90% and 98% degradation of dye, respectively after 90 minutes exposure to sunlight as shown in Fig. 15c. ZNC-(1 : 1 : 2) showed the maximum % dye degradation with highest rate constant value ($k = -3.934 \times 10^{-2}$ min^{-1}) which may be attributed to the smallest crystallite size of this NCP. The rate constant plot and values of 'k' are depicted in Fig. 15d.

4.1.2 Photodegradation of MO dye. Photodegradation of MO dye was also performed to check the catalytic behavior of NCPs for dyes other than MB. NCPs were found equally effective to photodegrade the MO dye as shown by the absorbance spectra ($\lambda_{max} = 464$ nm) (Fig. 16a) and color intensity (Fig. 16b) diagrams. Similar trend of dye degradation was observed *i.e.*,

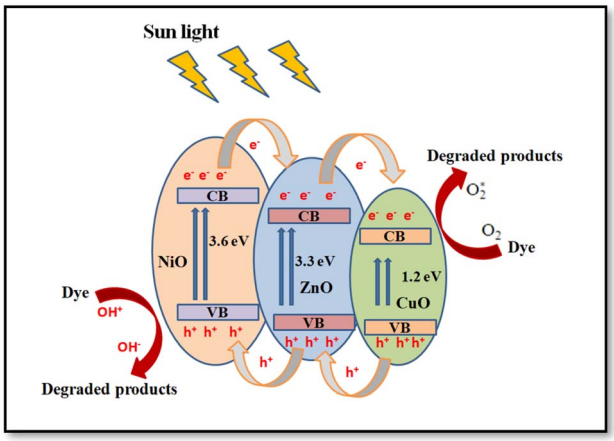

Fig. 18 Schematic diagram of ZnO–NiO–CuO NCPs heterojunctions for electron–hole pairs generation and segregation.

ZNC-(1 : 1 : 1), ZNC-(2 : 1 : 1), ZNC-(1 : 2 : 1) and ZNC-(1 : 1 : 2) exhibited 90%, 85%, 87% and 93% degradation of dye, respectively after 90 minutes exposure to sunlight as shown in Fig. 16c. Maximum dye degradation (93%) was observed in the presence of ZNC-(1 : 1 : 2) with highest rate constant value ($k = -2.920 \times 10^{-2}$ min^{-1}) which was attributed to the smallest crystallite size of this NCP. The rate constant plot and values of 'k' are depicted in Fig. 16d.

4.1.3 Photodegradation of mixture of dyes. Photodegradation of mixture of dyes (MB + MO) was carried out in presence of NCPs in the similar manner by addition of 20 mg of catalyst in each batch instead of 10 mg. The gradual decrease in the absorbance spectra of mixture of dyes (Fig. 17a) and color intensity (Fig. 17b) can be seen. NCPs showed the excellent capability to degrade the mixture of dyes by maximum degradation 92% (MB dye) and 88% (MO dye) shown by the ZNC-(1 : 1 : 2) NCP. The % dye degradation and rate constant plots of each NCP are shown in Fig. S5 and S6.† In environmental applications, the goal is often to treat wastewater or polluted water bodies that contain a mixture of pollutants. Investigating the photocatalytic degradation of a dye mixture directly addresses the practical need for efficient treatment solutions in such scenarios.

4.1.4 Generation and segregation of electron–hole pairs in NCPs. The change of molar ratios of metals in a NCP affects the photodegradation efficiency due to their influence on the NCP structure, morphology, and bandgap energy. These factors collectively affect the photodegradation process, leading to influence the overall efficiency of the degradation reaction. The combination of different metal oxides with different molar ratios can lead to a synergistic effect on photocatalytic activity. The presence of multiple metal ions can create new active sites, facilitate charge separation, and promote specific reactions, leading to improved performance.

Fig. 18 illustrates the formation of a heterojunction photocatalyst (ZnO–NiO–CuO) with distinct bandgap energies and band structures. This heterojunction interface enables efficient mobility and separation of photogenerated electrons and holes, reducing charge carrier recombination and maximizing photocatalytic activity. Furthermore, the smaller crystalline size in the 1 : 1 : 2 (Zn : Ni : Cu) molar ratio sample demonstrates the highest photodegradation efficiency (98% for MB and 93% for MO), while other samples show varying photodegradation efficiency based on their respective crystalline sizes. The remaining samples demonstrate a trend where the photodegradation efficiency varies in accordance with their respective crystalline sizes. This finding suggests a correlation between the size of the crystalline structure and the photocatalytic performance. The change in band gap resulting from different molar ratios, as observed in UV-vis spectra, may influence the degradation efficiency of dyes in photocatalytic processes.

In order to compare the photocatalytic potential of single, binary and mixed metal ternary oxides, batch wise photocatalytic decomposition of MB and MO dye solution was carried out under sunlight exposure of 90 minutes. From results of photodegradation of dyes (Table 6), it had been observed that the ternary metal oxides were more efficient for degradation of dyes, due to smaller bandgap, easy separation and less recombination of electron–hole pairs.

4.1.5 Effect of radical scavengers. In order to propose suitable mechanism of photodegradation and presence of main

Table 6 Comparison of photocatalytic potential of single, binary and ternary metal oxides

Material	Maximum degradation of MB (%)	Maximum degradation of MO (%)
ZnO NP	45	38
NiO NP	43	32
CuO NP	46	36
ZnO:NiO NC	75	72
ZnO:CuO NC	79	74
NiO:CuO NC	72	64
ZnO:NiO:CuO NC	98	93

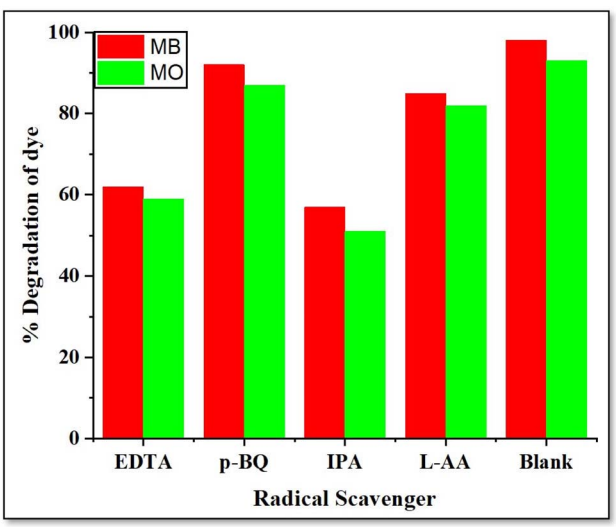

Fig. 19 Effect of radical scavengers on % dye degradation.

oxygen species involved in this process, radical scavenging/inhibition tests were carried out.[67,68] Four radical scavengers were used in batch experiments. Ethylenediaminetetraacetic acid (EDTA), *p*-benzoquinone (*p*-BQ), isopropanol (IPA) and L-ascorbic acid (L-AA) were used to scavenge holes (h^+), super oxide anion radical ($O_2^{\bullet -}$), hydroxyl radical ($OH^\bullet$) And hydrogen peroxide (H_2O_2), respectively.[68] 10 mL of 0.25 mM solution of each radical scavenger was added to the mixture of dye and catalyst in each catalytic batch experiment and decrease in % dye degradation was observed.

From Fig. 19, it can be observed that hydroxyl radicals and holes play major role in the photodegradation of dye because minimum % dye degradation was observed in presence of EDTA and IPA. Superoxide anion radical has minimum effect on degradation of dye followed by hydrogen peroxide. Collectively, all reactive oxygen species were produced in the mixture and contributed to dye degradation on surface of catalyst.

4.1.6 Proposed mechanism. During sunlight exposure, the photocatalyst having appropriate bandgap absorbs light energy to generate electron–hole pairs (e^-–h^+). Excited electrons in the CB reduce adsorbed pollutants, while holes in the VB oxidize them. This dual action of electron transfer and hole oxidation leads to the effective degradation of organic pollutants, transforming them into simpler and less harmful substances.[69] Thus, photocatalysis offers a promising approach to environmental purification. Proposed mechanism of action can be illustrated by the eqn (14)–(20).

$$\mathrm{ZnO\text{–}NiO\text{–}CuO} + h\nu \rightarrow \mathrm{ZnO\text{–}NiO\text{–}CuO}(e_{CB}^- + h_{VB}^+) \quad (14)$$

$$\mathrm{ZnO - NiO - CuO}(e_{CB}^-) + O_2 \rightarrow \mathrm{ZnO - NiO - CuO} + O_2^* \quad (15)$$

$$H_2O \rightarrow H^+ + OH^- \quad (16)$$

$$O_2^* + H^- \rightarrow HO_2^* \quad (17)$$

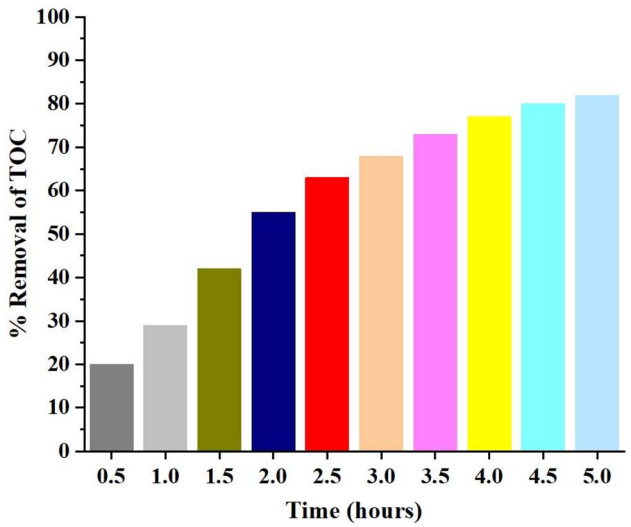

Fig. 20 % TOC removal of dye solution on catalyst surface.

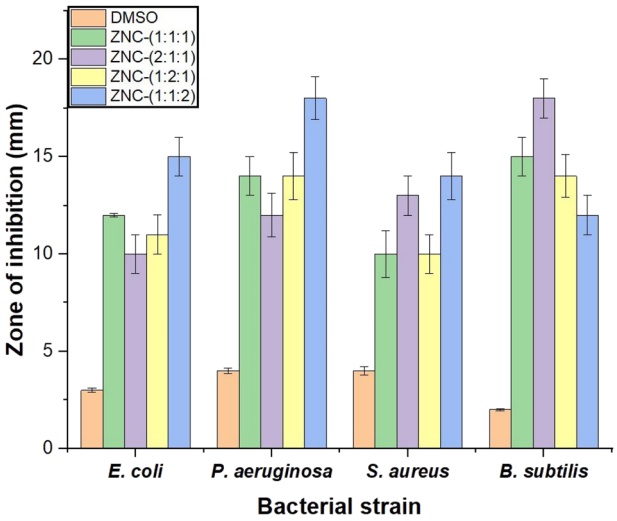

Fig. 21 ZOI of NCPs against different bacterial strains.

$$\mathrm{ZnO - NiO - CuO}(e_{CB}^-) + HO_2^* + H^+ \rightarrow H_2O_2 \quad (18)$$

$$\mathrm{ZnO\text{–}NiO\text{–}CuO}(h_{VB}^+) + \text{dye} \rightarrow \text{degradation product} \quad (19)$$

$$\mathrm{ZnO\text{–}NiO\text{–}CuO}(e_{CB}^-) + \text{dye} \rightarrow \text{degradation product} \quad (20)$$

Briefly, in the 1st step, electrons ae excited to the conduction band by absorption of light and electron–hole pair is generated. In 2nd step, photoexcited electron is used to reduce the oxygen molecule to oxygen radical which produces a chain of reactive radicals by reaction with water and other species. These excited radicals reduce the dye molecules by multiple secondary reactions while holes present in the valence band oxidize the dye molecules directly and cause degradation.

4.1.7 Total organic carbon analysis. Total organic carbon (TOC) analysis was carried out to analyze the extent of mineralization of dye on surface of catalyst.[70] Disappearance of color from the dye solution may be due to breakdown of azo group in the MO and MB which may result in the generation of more toxic species in solution. Therefore, it was pertinent to determine the carbon content analysis of solutions to determine how much mineralization has occurred.[71]

TOC analysis results are shown in Fig. 20. It shows that the mineralization lags behind the photodegradation process. % Removal of TOC value was measure after every 30 minutes up to 5 hours. 82% removal of TOC content was observed even after 5 hours which showed that the mineralization was relatively slower process and may take more time for 100% mineralization. Slow rate of mineralization process may be attributed to the breakdown of dye into many intermediates and slow oxidation of resistant nitrogen containing compounds produces as a result of azo group cleavage.

4.2 Antibacterial activity

The antibacterial activity of ZnO–NiO–CuO NCPs was evaluated using the disc diffusion method.[8] All the nanocomposites were

found effective to inhibit the growth of both bacterial strains *i.e.*, Gram-positive (*B. subtilis* and *S. aureus*) and Gram-negative (*E. coli* and *P. aeruginosa*). However, NCPs were found relatively more effective against Gram-negative strains with maximum inhibition shown by the ZNC-(1 : 1 : 2). More activity against the Gram-negative bacteria can be attributed to the different structure of cell wall of this strain. Cell wall of Gram-negative bacteria is relatively thin which result in the more penetration of small size NCPs in the cell, which resulted in the generation of reactive oxygen species (ROS) in the cell by interaction with different cell components. The ROS cause the inactivation of genetic material and proteins, which ultimately results in the death of bacteria.[72] The activity of each NCP to inhibit bacterial growth in terms of zone of inhibition is depicted in Fig. 21.

5. Conclusion

Ternary metal oxide NCPs (ZnO–NiO–CuO) were synthesized *via* the hydrothermal method, and their properties were studied by varying molar ratios *i.e.*, (Zn : Ni : Cu) 1 : 1 : 1, 2 : 1 : 1, 1 : 2 : 1, and 1 : 1 : 2. The XRD confirmed the presence of three phases in the NCPs. The volume fraction of metal oxides in the NCP was estimated by analyzing the relative intensity ratio of the peaks in PXRD and EDX spectra. Crystalline sizes and micro strains were determined using both Scherrer and W–H methods. The crystallite sizes of 21 nm, 27 nm, 23 nm, and 20 nm were observed for the molar ratios 1 : 1 : 1, 2 : 1 : 1, 1 : 2 : 1, and 1 : 1 : 1, respectively, attributed to the unique ionic radii of the metals present in the NCP. The FTIR spectra analysis of the NCPs confirmed the presence of vibrational peaks corresponding to the –OH, Zn–O, Ni–O, and Cu–O bonds. The UV-vis analysis demonstrated that altering the molar ratios resulted in a modification of the bandgap due to the varying bandgaps of the constituent metal oxides. SEM images of the synthesized NCPs exhibited agglomerated mixed rod and spherical-like nanostructures. TGA showed the high stability of NCPs at high temperature with minimum weight loss (%). DC electrical measurements demonstrated that the NCPs exhibited high electrical conductivity and low activation energies by increased molar ratios present in the NCPs due to an increase in the availability of charge carriers (electrons or holes) within the NCP. The analysis of dielectric properties of the NCPs revealed that NCPs have higher dielectric constant and tangent loss at low frequencies, and then gradually decrease with increasing electric field frequency. By increasing the molar ratios, the concentration of metal ions increased in ZnO–NiO–CuO NCPs resulting in increased dielectric constant due to higher charge carrier density and polarization response. The NCP with a molar ratio of 1 : 1 : 2 exhibited the highest photodegradation efficiency for degradation of MB (98%), MO (93%) and mixture of dyes (92% MB and 88% MO) due to its smaller crystallite size and higher surface energies, facilitating enhanced photocatalytic activity. The antibacterial property of NCPs revealed the crystallite size dependent inhibition of bacterial strains. The comprehensive study of applications of this material proves the commercial importance of this material for purification of water.

Data availability

All the data is available in the manuscript. Additional information/data can be provided on request.

Conflicts of interest

The authors have no relevant financial or non-financial interests to disclose.

Acknowledgements

The authors extend their appreciation to Researchers Supporting Project number (RSP2023R165), King Saud University, Riyadh, Saudi Arabia.

References

1 B. A. Anderson, J. H. Romani, H. Phillips, M. Wentzel and K. Tlabela, *Popul. Environ.*, 2007, **28**, 133–161.
2 Y. Hunge, A. Yadav, S.-W. Kang and H. Kim, *J. Alloys Compd.*, 2022, **928**, 167133.
3 Y. Cui, C. Lin, M. Li, N. Zhu, J. Meng and J. Zhao, *J. Alloys Compd.*, 2022, **893**, 162181.
4 X. Jv, X. Zhao, H. Ge, J. Sun, H. Li, Q. Wang and H. Lu, *J. Chem. Eng. Data*, 2019, **64**, 1228–1236.
5 S. R. Yousefi, A. Sobhani, H. A. Alshamsi and M. Salavati-Niasari, *RSC Adv.*, 2021, **11**, 11500–11512.
6 H. Zhang, B. Xia, P. Wang, Y. Wang, Z. Li, Y. Wang, L. Feng, X. Li and S. Du, *J. Alloys Compd.*, 2020, **819**, 153053.
7 S. Gunatilake, *Methods*, 2015, **1**, 14.
8 M. Z. Ishaque, Y. Zaman, M. Shahzad, A. B. Siddique, S. Shahid, M. Akram, H. Kanwal, M. T. Akhtar and S. Hussain, *Water, Air, Soil Pollut.*, 2023, **234**, 252.
9 K. Qi, B. Cheng, J. Yu and W. Ho, *J. Alloys Compd.*, 2017, **727**, 792–820.
10 Y. Zaman, M. Z. Ishaque, S. Ajmal, M. Shahzad, A. B. Siddique, M. U. Hameed, H. Kanwal, R. J. Ramalingam, M. Selvaraj and G. Yasin, *Inorg. Chem. Commun.*, 2023, 110523.
11 M. Lines, *J. Alloys Compd.*, 2008, **449**, 242–245.
12 C. B. Ong, L. Y. Ng and A. W. Mohammad, *Renewable Sustainable Energy Rev.*, 2018, **81**, 536–551.
13 A. Mishra, A. Mehta and S. Basu, *J. Environ. Chem. Eng.*, 2018, **6**, 6088–6107.
14 K. Kannan, D. Radhika, M. P. Nikolova, K. K. Sadasivuni, H. Mahdizadeh and U. Verma, *Inorg. Chem. Commun.*, 2020, **113**, 107755.
15 A. K. Sibhatu, G. K. Weldegebrieal, S. Sagadevan, N. N. Tran and V. Hessel, *Chemosphere*, 2022, **300**, 134623.
16 G. Elango and S. M. Roopan, *J. Photochem. Photobiol., B*, 2016, **155**, 34–38.
17 M. Tariq, Y. Zaman, M. Shahzad, K. Ahmad, A. B. Siddique and H. Zaman, *Mater. Sci. Eng., B*, 2023, **294**, 116549.
18 I. Jabbar, Y. Zaman, K. Althubeiti, S. Al Otaibi, M. Z. Ishaque, N. Rahman, M. Sohail, A. Khan, A. Ullah and T. Del Rosso, *RSC Adv.*, 2022, **12**, 13456–13463.

19 C. M. Magdalane, K. Kanimozhi, M. Arularasu, G. Ramalingam and K. Kaviyarasu, *Surf. Interfaces*, 2019, **17**, 100346.
20 T.-P. Ruoko, K. Kaunisto, M. Bärtsch, J. Pohjola, A. Hiltunen, M. Niederberger, N. V. Tkachenko and H. Lemmetyinen, *J. Phys. Chem. Lett.*, 2015, **6**, 2859–2864.
21 M. B. Mobarak, M. S. Hossain, F. Chowdhury and S. Ahmed, *Arabian J. Chem.*, 2022, **15**, 104117.
22 W. Ye, Y. Jiang, Q. Liu, D. Xu, E. Zhang, X. Cheng, Z. Wan and C. Liu, *J. Alloys Compd.*, 2022, **891**, 161898.
23 P. Panchal, D. R. Paul, A. Sharma, D. Hooda, R. Yadav, P. Meena and S. Nehra, *J. Photochem. Photobiol., A*, 2019, **385**, 112049.
24 M. A. Subhan, T. Ahmed, N. Uddin, A. K. Azad and K. Begum, *Spectrochim. Acta, Part A*, 2015, **136**, 824–831.
25 X. Li, R. Zhao, H. Jiang, Y. Zhai and P. Ma, *Synth. React. Inorg., Met.-Org., Nano-Met. Chem.*, 2016, **46**, 775–782.
26 T. Munawar, F. Mukhtar, M. S. Nadeem, S. Manzoor, M. N. Ashiq, K. Mahmood, S. Batool, M. Hasan and F. Iqbal, *J. Alloys Compd.*, 2022, **898**, 162779.
27 T. Munawar, S. Yasmeen, F. Hussain, K. Mahmood, A. Hussain, M. Asghar and F. Iqbal, *Mater. Chem. Phys.*, 2020, **249**, 122983.
28 O. Çomakli, M. Yazici, T. Yetim, F. Yetim and A. Celik, *Ind. Lubr. Tribol.*, 2019, **71**, 1166–1176.
29 M. Rezaei and A. Nezamzadeh-Ejhieha, *Int. J. Hydrogen Energy*, 2020, **45**, 24749–24764.
30 D. Paul, S. Mangla and S. Neogi, *Mater. Lett.*, 2020, **271**, 127740.
31 C. Zhang, L. Yin, L. Zhang, Y. Qi and N. Lun, *Mater. Lett.*, 2012, **67**, 303–307.
32 M. Srinivasan and N. Punithavelan, *Mater. Res. Express*, 2018, **5**, 075033.
33 R. Sattara, M. Rasoola, R. Qadirb, A. Siddiqueb, M. Irfanb, I. Sabac, M. Akhtarb, M. ur Rehmana and M. Mustaqeemb, *J. Optoelectron. Biomed. Mater.*, 2023, **15**, 1–9.
34 Y. Zamana, M. Ishaquea, R. Sattarb, M. Rehmanb, I. Sabac, S. Kanwala, M. Akrama, M. Shahzada, H. Kanwald and R. Qadirb, *Dig. J. Nanomater. Biostructures*, 2022, **17**, 979–987.
35 A. B. Siddique, S. Ahmad, M. A. Shaheen, A. Ali, M. N. Tahir, L. C. Vieira, S. Muhammad and S. M. Siddeeg, *CrystEngComm*, 2022, **24**(47), 8237–8247.
36 M. S. Ahmad, A. B. Siddique, M. Khalid, A. Ali, M. A. Shaheen, M. N. Tahir, M. Imran, A. Irfan, M. U. Khan and M. W. Paixão, *RSC Adv.*, 2023, **13**, 9222–9230.
37 A. Jafari, S. P. Jahromi, K. Boustani, B. T. Goh and N. M. Huang, *J. Magn. Magn. Mater.*, 2019, **469**, 383–390.
38 A. George, D. M. A. Raj, A. D. Raj, A. A. Irudayaraj, J. Arumugam, H. J. Prabu, S. J. Sundaram, N. A. Al-Dhabi, M. V. Arasu and M. Maaza, *Surf. Interfaces*, 2020, **21**, 100761.
39 R. Kadam, R. Borade, M. Mane, D. Mane, K. Batoo and S. E. Shirsath, *RSC Adv.*, 2020, **10**, 27911–27922.
40 D. Perwitasari, S. Muryanto, J. Jamari and A. Bayuseno, *J. Environ. Chem. Eng.*, 2018, **6**, 37–43.
41 A. Dolgormaa, C.-j. Lv, Y. Li, J. Yang, J.-x. Yang, P. Chen, H.-p. Wang and J. Huang, *Molecules*, 2018, **23**, 2982.
42 A. Jayachandran, T. Aswathy and A. S. Nair, *Biochem. Biophys. Rep.*, 2021, **26**, 100995.
43 A. J. Ahamed, P. V. Kumar and M. Karthikeyan, *Int. J. Nano Corros. Sci. Eng.*, 2015, **2**, 31–38.
44 E. Da'na, A. Taha and M. Hessien, *Ceram. Int.*, 2021, **47**, 4531–4542.
45 P. Muhambihai, V. Rama and P. Subramaniam, *J. Adv. Sci. Res.*, 2020, **11**, 358–364.
46 P. Muhambihai, V. Rama and P. Subramaniam, *Environ. Nanotechnol., Monit. Manage.*, 2020, **14**, 100360.
47 Z. Biglari, S. Masoudpanah and S. Alamolhoda, *J. Electron. Mater.*, 2018, **47**, 2703–2709.
48 P. Makuła, M. Pacia and W. Macyk, *J. Phys. Chem. Lett.*, 2018, **9**, 6814–6817.
49 S. Javaid, M. A. Farrukh, I. Muneer, M. Shahid, M. Khaleeq-ur-Rahman and A. A. Umar, *Superlattices Microstruct.*, 2015, **82**, 234–247.
50 Y. Yoon, P. L. Truong, D. Lee and S. H. Ko, *ACS Nanosci. Au*, 2021, **2**, 64–92.
51 M. Ibrahim, A. Latif, M. Ahmad, S. Ahmad, A. Ali, A. B. Siddique, M. Saadiq, N. Akbar, A. Khan and A. Al-Harrasi, *J. Mol. Struct.*, 2021, 132215.
52 Y. Zaman, M. Z. Ishaque, K. Waris, M. Shahzad, A. B. Siddique, M. I. Arshad, H. Zaman, H. M. Ali, F. Kanwal, M. Aslam and M. Mustaqeem, *Arabian J. Chem.*, 2023, 105230.
53 S. Bagheri, K. Chandrappa and S. Hamid, *Pharma Chem.*, 2013, **5**, 265–270.
54 N. Tamaekong, C. Liewhiran and S. Phanichphant, *J. Nanomater.*, 2014, **2014**, 6.
55 M. Dinesha, H. Jayanna, S. Ashoka and G. Chandrappa, *J. Alloys Compd.*, 2009, **485**, 538–541.
56 K. Omri, I. Najeh and L. El Mir, *Ceram. Int.*, 2016, **42**, 8940–8948.
57 A. Bakri, M. Z. Sahdan, F. Adriyanto, N. Raship, N. Said, S. Abdullah and M. Rahim, *AIP Conf. Proc.*, 2017, **1788**, 1–9.
58 S.-Y. Kuo, W.-C. Chen, F.-I. Lai, C.-P. Cheng, H.-C. Kuo, S.-C. Wang and W.-F. Hsieh, *J. Cryst. Growth*, 2006, **287**, 78–84.
59 P. G. Undre, S. D. Birajdar, R. Kathare and K. Jadhav, *Procedia Manuf.*, 2018, **20**, 477–480.
60 M. Arshad, A. Maqsood, I. Gul and M. Anis-Ur-Rehman, *Mater. Res. Bull.*, 2017, **87**, 177–185.
61 M. Ashokkumar and S. Muthukumaran, *Powder Technol.*, 2014, **268**, 80–85.
62 T. Prodromakis and C. Papavassiliou, *Appl. Surf. Sci.*, 2009, **255**, 6989–6994.
63 M. Akram, A. Javed and T. Z. Rizvi, *Turk. J. Phys.*, 2005, **29**, 355–362.
64 M. Lakhane, K. Bogle, R. Khairnar, S. Dahiwale, R. Sharma, V. Mokale and M. Mahabole, *Nano-Struct. Nano-Objects*, 2019, **17**, 248–258.
65 H. Bouaamlat, N. Hadi, N. Belghiti, H. Sadki, M. Naciri Bennani, F. Abdi, T.-d. Lamcharfi, M. Bouachrine and M. Abarkan, *Adv. Mater. Sci. Eng.*, 2020, **2020**, 1–8.
66 İ. Taşçıoğlu, Ö. T. Özmen, H. Şağban, E. Yağlıoğlu and Ş. Altındal, *J. Electron. Mater.*, 2017, **46**, 2379–2386.

67 X. Zheng, J. Yuan, J. Shen, J. Liang, J. Che, B. Tang, G. He and H. Chen, *J. Mater. Sci.: Mater. Electron.*, 2019, **30**, 5986–5994.
68 N. Skillen, C. Rice, X. Pang, P. K. Robertson, W. McCormick and D. McCrudden, *Nanostruct. Photocatal.*, 2021, 85–118.
69 A. Ajmal, I. Majeed, R. N. Malik, H. Idriss and M. A. Nadeem, *RSC Adv.*, 2014, **4**, 37003–37026.
70 I. K. Konstantinou and T. A. Albanis, *Appl. Catal., B*, 2004, **49**, 1–14.
71 W. W. Anku, S. O.-B. Oppong, S. K. Shukla and P. P. Govender, *Acta Chim. Slov.*, 2016, **63**, 380–391.
72 N. El-Shafai, M. E. El-Khouly, M. El-Kemary, M. Ramadan, I. Eldesoukey and M. Masoud, *RSC Adv.*, 2019, **9**, 3704–3714.